


 Cite this: *RSC Adv.*, 2024, 14, 19124

# Ion migration and dark current suppression in quasi-2D perovskite-based X-ray detectors†

 Zhenting Yang,<sup>a</sup> Aimiao Qin,<sup>b</sup> Haiqing Qin,<sup>c</sup> Zhenlin Li,<sup>d</sup> Yong Xiang,<sup>ae</sup> Hao Liu,<sup>f</sup> Jinyu Qiu<sup>g</sup> and Xinyu Wang<sup>ib</sup>\*<sup>a</sup>

Cesium-based lead-free double perovskite materials ( $\text{Cs}_2\text{AgBiBr}_6$ ) have garnered significant attention in the X-ray detection field due to their environment friendly characteristics. However, their substantial ion migration properties lead to large dark currents and detection limits in  $\text{Cs}_2\text{AgBiBr}_6$ -based X-ray detectors, restricting the detection performance of the device. In terms of process technology, ultrasonic spraying is more suitable than a spin-coating method for fabricating large-area, micron-scale perovskite thick films, with higher cost-effectiveness, which is crucial for X-ray detection. This work introduces a  $\text{BA}^+$  ( $\text{BA}^+ = \text{CH}_3\text{CH}_2\text{CH}_2\text{CH}_2\text{NH}_3^+$ , *n*-butyl) source into the precursor solution and employs ultrasonic spraying to fabricate quasi-two-dimensional structured polycrystalline  $(\text{BA})_2\text{Cs}_9\text{Ag}_5\text{Bi}_5\text{Br}_{31}$  perovskite thick films, developing a low-cost, eco-friendly X-ray detector with low dark current density and low detection limit. Characterization results reveal that the ion migration activation energy of  $(\text{BA})_2\text{Cs}_9\text{Ag}_5\text{Bi}_5\text{Br}_{31}$  reaches 419 meV, approximately 17% higher than that of traditional three-dimensional perovskites, effectively suppressing perovskite ion migration and subsequently reducing the dark current. The  $(\text{BA})_2\text{Cs}_9\text{Ag}_5\text{Bi}_5\text{Br}_{31}$ -based X-ray detectors exhibit high resistivity (about  $1.75 \times 10^{10} \Omega \text{ cm}$ ), low dark current density ( $66 \text{ nA cm}^{-2}$ ), minimal dark current drift ( $0.016 \text{ pA cm}^{-1} \text{ s}^{-1} \text{ V}^{-1}$ ), and detection limit ( $138 \text{ nGy}_{\text{air}} \text{ s}^{-1}$ ), holding considerable promise for applications in low-noise, low-dose X-ray detection.

Received 7th April 2024

Accepted 10th June 2024

DOI: 10.1039/d4ra02606c

[rsc.li/rsc-advances](https://rsc.li/rsc-advances)

## 1. Introduction

As the era progresses, with the development of technology and the increasing needs of people, high-energy ionizing radiation X-ray detection technology plays a crucial role in fields such as medical imaging, security imaging, and industrial non-destructive testing.<sup>1–3</sup> Among current X-ray direct detection technologies, commercial detectors employing amorphous selenium ( $\alpha\text{-Se}$ ) as the photoabsorbing layer have been developed.<sup>4</sup> However, due to their lower carrier mobility-lifetime product, lower atomic number, and the need for a higher

operating electric field for effective operation, they exhibit lower sensitivity and higher detection limits in practical applications.<sup>5</sup> Other traditional semiconductor materials, such as cadmium telluride ( $\text{CdTe}$ ) and cadmium zinc telluride ( $\text{CdZnTe}$ ), offer higher absorption rates for high-energy X-Rays compared to amorphous selenium, but these materials require high-temperature melting methods for preparation, making them relatively expensive.<sup>6</sup> The development of new materials is urgently needed to meet high-performance detection requirements while also considering cost and fabrication process optimizations.

Halide perovskite materials, since their introduction, have not only demonstrated excellent photoelectric conversion efficiency in the photovoltaic field but also meet the requirements for high-performance X-ray detection due to their high X-ray absorption coefficient, high carrier mobility-lifetime product  $\mu\tau$ , large resistivity, and low cost.<sup>7–9</sup> Among the halide perovskites reported, lead-based halides containing high atomic number Pb elements, have stronger X-ray absorption capabilities, resulting in high sensitivity devices, and have long been a hot research material in the field.<sup>10,11</sup> However, the toxic nature of lead poses certain barriers to their commercial development.

Lead-free double perovskite  $\text{Cs}_2\text{AgBiBr}_6$  single crystals have shown excellent X-ray response performance while meeting green and environment friendly requirements. Tang Jiang's team<sup>12</sup> pioneered the development of X-ray direct detectors

<sup>a</sup>School of Materials and Energy, University of Electronic Science and Technology of China, Chengdu, China. E-mail: xinyuwang@uestc.edu.cn

<sup>b</sup>Key Laboratory of New Processing Technology for Nonferrous Metal & Materials, Ministry of Education/Guangxi Key Laboratory of Optical and Electronic Materials and Devices, Guilin University of Technology, Guilin, China

<sup>c</sup>Guangxi Key Laboratory of Superhard Material, National Engineering Research Center for Special Mineral Material, Guangxi Technology Innovation Center for Special Mineral Material, China Nonferrous Metal (Guilin) Geology And Mining Co., Ltd, Guilin, China

<sup>d</sup>Department of Radiology, West China Hospital, Sichuan University, Chengdu, China

<sup>e</sup>Tianfu Jiangxi Laboratory, Chengdu, China

<sup>f</sup>BOE Technology Group Co., Ltd, Beijing, China

<sup>g</sup>Chengdu Experimental Foreign Languages School International Department, Chengdu, Sichuan, China

† Electronic supplementary information (ESI) available. See DOI: <https://doi.org/10.1039/d4ra02606c>



based on  $\text{Cs}_2\text{AgBiBr}_6$  single crystals grown *via* a low-cost solution, achieving a detector sensitivity of  $105 \mu\text{C Gy}_{\text{air}}^{-1} \text{cm}^{-2}$  and a minimum detection limit of  $59.7 \text{ nGy}_{\text{air}} \text{ s}^{-1}$ , with good thermal and radiation stability. This discovery provides an important material basis for the development of efficient and environment friendly X-ray detectors. In fact, the preparation process of single crystals is relatively complex and has low compatibility with the transistor (TFT) backplane used in the imaging end. Compared to single crystals, polycrystalline thick films are more suitable for low-cost and large-area X-ray detection applications.<sup>13</sup> Despite significant progress in perovskite-based X-ray detectors, challenges remain due to the intrinsic ion migration within perovskite compounds. Charged ions within the material can be driven by external electric fields, leading to ion migration along defects and other channels, which can generate significant noise and baseline drift issues, adverse for achieving lower detection limits and high stability devices.<sup>14</sup> Especially in polycrystalline materials, the vast number of grain boundaries makes ions more inclined to migrate along defects at the boundaries, further exacerbating noise and baseline drift issues. Therefore, further suppression of ion migration in polycrystalline perovskites is key to achieving high stability X-ray detectors.

Studies have found that for perovskite polycrystalline films, various methods such as producing a thick film with a compact structure<sup>15,16</sup> to reduce voids, growing large-size grains,<sup>17</sup> passivating grain boundaries,<sup>18</sup> and dimension control,<sup>19</sup> can reduce ion migration in perovskite materials. Among these, a widely studied method in dimension control strategies involves adding large organic cations (such as phenethylammonium,  $\text{PEA}^+$ ,<sup>20</sup> butylammonium,  $\text{BA}^+$ ,<sup>21</sup> *etc.*) to the perovskite precursor solution. This separates part of the  $[\text{BX}_6]^{4-}$  octahedra originally connected in a vertex-sharing manner in the three-dimensional perovskite structure, relying on van der Waals forces between organic cations to stably combine, thereby inducing a layered RP structure  $\text{A}'_2\text{A}_{n-1}\text{B}_n\text{X}_{3n+1}$  (where  $\text{A}'$  is a substituted large-size organic cation,  $\text{A}$  is an inorganic cation group,  $\text{B}$  is a high atomic number metal cation like  $\text{Pb}^{2+}$  or  $\text{Sn}^{2+}$ , and  $\text{X}$  is one or a combination of halogen ions such as  $\text{I}^-$ ,  $\text{Br}^-$ ,  $\text{Cl}^-$ , with  $n$  representing the number of inorganic octahedral layers, *i.e.*, the inorganic layer number in low-dimensional perovskites). In 2022, Yukta and others<sup>22</sup> successfully prepared X-ray detectors based on pure two-dimensional RP structure  $(\text{BA})_2\text{PbI}_4$  single crystals, featuring high resistivity of  $2.60 \times 10^{11} \Omega \text{ cm}$  and a low detection limit of  $241 \text{ nGy}_{\text{air}} \text{ s}^{-1}$ , demonstrating excellent radiation and environmental stability. In the same year, Zhang and others<sup>23</sup> adjusted the dimension of RP perovskite materials by the reaction between methylamine gas and the RP perovskite precursor, achieving a high degree of control over ion migration characteristics in perovskites through  $\text{BA}_2\text{MA}_{n-1}\text{Pb}_n\text{I}_{3n+1} \cdot x\text{CH}_3\text{NH}_2$  series perovskites. This low-dimensional structure design of interlaced organic and inorganic layers effectively blocks ion migration pathways at the microscopic level, significantly suppressing ion migration capability.

Xu and others<sup>21</sup> obtained  $(\text{BA})_2\text{CsAgBiBr}_7$  with a quasi two-dimensional structure from a saturated solution using temperature cooling technology, and generated a sensitivity of

$4.2 \mu\text{C Gy}_{\text{air}}^{-1} \text{cm}^{-2}$  under an X-ray source, laying the foundation for the application of low dimensional double perovskite  $\text{Cs}_2\text{AgBiBr}_6$  materials in the field of X-ray detection. Zhang and others<sup>24</sup> prepared a quasi two-dimensional structure of  $(\text{BA})_2\text{CsAgBiBr}_7$  by introducing organic cation  $\text{BA}^+$ , and grown centimeter level lead-free perovskite heterocrystals:  $(\text{BA})_2\text{CsAgBiBr}_7/\text{Cs}_2\text{AgBiBr}_6$  through *in situ* epitaxy technology, exhibiting a high sensitivity of  $206 \mu\text{C Gy}_{\text{air}}^{-1} \text{cm}^{-2}$ . Although these studies demonstrate the enormous potential of quasi two-dimensional perovskites in the field of X-ray detection, they further demonstrate the enormous potential of quasi two-dimensional perovskite materials in the field of X-ray detection. However, most of the studies on low dimensional materials of  $\text{Cs}_2\text{AgBiBr}_6$  mainly focused on single crystal materials, which are difficult to meet the needs of X-ray detection applications for large-area growth due to their small size. In fact, polycrystalline thick films are more suitable for low-cost, large-area X-ray detection scenarios than single crystal materials. Nonetheless, research reports on dimension control of polycrystalline  $\text{Cs}_2\text{AgBiBr}_6$  materials remain relatively scarce. Therefore, we have made improvements to address the shortcomings of existing research and systematically explored the potential of quasi two-dimensional double perovskite polycrystalline materials in X-ray detection applications.

This study adds the large organic molecule butylammonium cation  $\text{BA}^+$  to the three-dimensional perovskite  $\text{Cs}_2\text{AgBiBr}_6$  precursor solution, constructing a quasi-two-dimensional perovskite structure, and uses ultrasonic spraying (Note 1, ESI†) to prepare polycrystalline thick films with different inorganic layer numbers  $n$  on conductive substrates. Through systematic characterization of the film's morphology, orientation, and element distribution, the study investigates the control mechanism of butylammonium bromide  $\text{BABr}$  introduction on the crystal dimension of  $\text{Cs}_2\text{AgBiBr}_6$  perovskite polycrystalline thick films. The study shows that<sup>25</sup> the introduction of  $\text{BA}^+$  from  $\text{BABr}$  leads to the transformation of  $\text{Cs}_2\text{AgBiBr}_6$  into an  $\text{A}'_2\text{A}_{n-1}\text{B}_n\text{X}_{3n+1}$  RP-type quasi-two-dimensional structure, where  $n$  represents the number of inorganic layers between the organic spacing cations  $\text{BA}^+$ . This work synthesized  $n = \infty$  (which is pure  $\text{Cs}_2\text{AgBiBr}_6$ ),  $n = 10$  (which is  $(\text{BA})_2\text{Cs}_9\text{Ag}_5\text{Bi}_5\text{Br}_{31}$ ), and  $n = 6$  (which is  $(\text{BA})_2\text{Cs}_5\text{Ag}_3\text{Bi}_3\text{Br}_{19}$ ) dual perovskite systems, with the material's quasi-two-dimensional inorganic layer number inversely related to  $n$ , *i.e.*, the smaller the  $n$  value, the more inorganic layers in the  $\text{Cs}_2\text{AgBiBr}_6$  perovskite system. The article systematically studies the relationship between different inorganic layer numbers and their ion migration characteristics, selecting the quasi-two-dimensional cesium-based double perovskite system  $(\text{BA})_2\text{Cs}_9\text{Ag}_5\text{Bi}_5\text{Br}_{31}$  with the highest activation energy. Based on this material system, an X-ray detector was fabricated, successfully suppressing dark current and lowering the detection limit.

## 2. Method

### 2.1 Materials

Cesium bromide ( $\text{CsBr}$ , 99.999%) was purchased from Xi'an Bathsun Energy Technology Co., Ltd, silver bromide ( $\text{AgBr}$ ,



98%), bismuth bromide ( $\text{BiBr}_3$ ,  $\geq 98\%$ ), butylammonium bromide ( $n\text{-BABr}$ ,  $>98.0\%$ ), dimethyl sulfoxide (DMSO,  $>99.8\%$  (GC)),  $N,N$ -dimethylformamide (DMF, anhydrous grade), and polyvinylpyrrolidone (PVP, K60) were obtained from Aladdin Reagent Co., Ltd. All materials were used as received without further purification.

## 2.2 Material synthesis

0.6 g of PVP was dissolved in 5 ml of DMF and stirred at  $50\text{ }^\circ\text{C}$  in a water bath for 5 hours to obtain a PVP solution. Then, a PVP thin film was formed on the substrate *via* spin-coating as an intermediate layer and was cross-linked and kept warm in a vacuum oven for 0.5 hours. The spin-coating parameters were set as follows: first spin-coated at 700 rpm for 7 seconds, then at 3000 rpm for 3 seconds.

For the preparation of quasi-two-dimensional perovskites with different inorganic layer numbers, according to the general chemical formula  $\text{A}'_2\text{A}_{n-1}\text{B}_n\text{X}_{3n+1}$ , the stoichiometric ratio of components was adjusted.<sup>26</sup> CsBr, AgBr,  $\text{BiBr}_3$ , and  $n\text{-BABr}$  powders were mixed in the required molar ratio to prepare precursor solutions for cesium-based lead-free perovskites with  $n = 6$  (*i.e.*,  $(\text{BA})_2\text{Cs}_5\text{Ag}_3\text{Bi}_3\text{Br}_{19}$ ) and  $n = 10$  (*i.e.*,  $(\text{BA})_2\text{Cs}_9\text{Ag}_5\text{Bi}_5\text{Br}_{31}$ ). Here,  $\text{A}'$  represents the organic cation  $\text{BA}^+$  substituting the inorganic A-site cation  $\text{Cs}^+$ , and B denotes Ag or Bi.

Taking  $n = 10$ , *i.e.*,  $(\text{BA})_2\text{Cs}_9\text{Ag}_5\text{Bi}_5\text{Br}_{31}$  quasi-two-dimensional perovskite as an example, 3.06 g CsBr, 1.50 g AgBr, 3.59 g  $\text{BiBr}_3$ , and 0.49 g  $n\text{-BABr}$  were weighed and added into a clean glass bottle, dissolved in 40 ml DMSO, and the bottle was sealed and stirred overnight on a magnetic stirrer. After the perovskite solution became homogeneous without floating particles, 40 ml of DMF was added, and the mixture was stirred for 3 hours to obtain a clear, transparent perovskite precursor solution.

Secondly, a three-dimensional structure  $\text{Cs}_2\text{AgBiBr}_6$  perovskite, *i.e.*,  $n = \infty$ , was prepared as the control group for this study. 3.40 g CsBr, 1.50 g AgBr, 3.59 g  $\text{BiBr}_3$  powders were dissolved in 40 ml DMSO, and after overnight stirring, 40 ml DMF was added to dilute the original solution.

Different inorganic layer numbers ( $n = \infty$ , 10, and 6) of perovskite light-absorbing layers were prepared using ultrasonic spray coating, with a working power set to 2.5 W to atomize the precursor solution, assisted by nitrogen gas, and the substrate temperature was set to  $140\text{ }^\circ\text{C}$ . After deposition, the samples were cooled to room temperature at a rate of  $1\text{ }^\circ\text{C min}^{-1}$ .

## 2.3 Device fabrication

Metal upper electrodes were fabricated using a silver paste scraping method to construct ITO/PVP/Perovskite/Ag devices for subsequent characterization and testing, where PVK denotes the perovskite light-absorbing layer. A mask with an electrode area of  $0.02\text{ cm}^2$  was selected as the scraping tool. Before scraping, the mask was ultrasonically cleaned in anhydrous ethanol for 15 minutes and dried with a nitrogen gun. The mask was fixed above the sample with tape, and an appropriate amount of silver paste was applied through the electrode area of

the mask and evenly scraped on the sample surface. After scraping, the device was immediately placed in an oven to dry at  $60\text{ }^\circ\text{C}$  for 3 hours.

## 2.4 Characterization

Phase analysis of the samples was conducted using a Rigaku SmartLab SE X-ray diffraction (XRD) instrument with Cu target  $K\alpha$  radiation. A MERLIN Compact field emission scanning electron microscope (SEM) from ZEISS, Germany, was used, and energy-dispersive spectroscopy (EDS) tests were performed on the same equipment to analyze the micro-surface morphology, cross-sectional information, and element distribution. A Keithley electrometer, model 6517B, was used to measure the device's dark current and ionic conductivity, studying the material's ion migration characteristics. The response and detection limit of the detector to X-Rays were obtained by irradiating the sample with X-Rays from an X-ray tube, reading, and collecting signal data through a probe station and Keithley electrometer.

## 3. Results and discussion

We synthesized a series of perovskite film with thicknesses in the micron range for  $n = \infty$ , 10, and 6, where  $n$  represents the number of inorganic octahedral layers. For perovskite thick films with low  $n$ -value (*e.g.*,  $n = 1$  and  $n = 2$ ), more organic components hinder solvent evaporation and leads to excessive interfaces and defects during the formation (Fig. S1, ESI<sup>†</sup>). Additionally, these materials demonstrated high dark current densities (Fig. S4(a) and (b), ESI<sup>†</sup>). For perovskite thick films with higher  $n$ -value,  $n = 14$  was found that its resistivity was similar to that of traditional three-dimensional perovskite (Fig. S4(c), ESI<sup>†</sup>). This indicates that materials with higher  $n$ -values are similar to three-dimensional perovskites, losing the specific advantages of quasi two-dimensional structures.

### 3.1 Phase analysis

X-Ray diffraction (XRD) can be used to determine the orientation and crystallinity of perovskite thick films. Fig. 1 presents the XRD patterns and a magnified view for samples with different inorganic layer numbers  $n$ . As can be seen from Fig. 1(a), under the intercalation effect of the  $n\text{-BABr}$  organic molecule, the perovskite thick films of  $n = \infty$ ,  $n = 10$ , and  $n = 6$  show no extra impurity peaks, indicating high phase purity of the materials, which is beneficial for the transport of carriers within the materials. In the low-angle ( $2\theta < 10^\circ$ ) diffraction peak range for  $n = 10$  and  $n = 6$ , a distinct diffraction peak emerges, as the large organic cations first induce the crystal to crystallize along the (002) plane,<sup>24</sup> the presence of the low diffraction angle peak confirms the formation of low-dimensional perovskites, consistent with XRD results of quasi-two-dimensional perovskite materials reported in other studies.<sup>23</sup> Fig. 1(b) is a magnified view of the (002) plane diffraction angle around  $6.50^\circ$  from Fig. 1(a), where the full width at half maximum (FWHM) at this diffraction peak for different  $n$  values can be clearly observed. The FWHMs for  $n = 10$  and  $n = 6$  thick films are  $0.141^\circ$  and



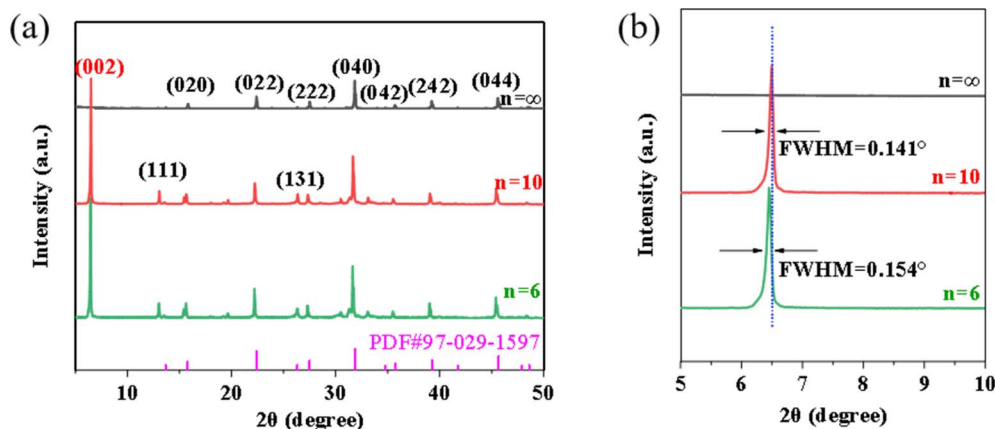


Fig. 1 (a) XRD spectra of different  $n$ -values of perovskite; (b) XRD spectra of enlarged (200) plane.

0.154°, respectively, reflecting changes in the average grain size of the materials. According to the Scherrer formula:<sup>27</sup>

$$D = \frac{K\lambda}{B \cos \theta} \quad (1)$$

where  $D$  represents the average grain size of the sample;  $K$  is the Scherrer constant;  $\lambda$  is the wavelength of X-Rays;  $B$  is the FWHM;  $\theta$  is the diffraction angle. By applying the Scherrer formula, the average grain sizes for the  $n = 10$  and  $n = 6$  thick films are calculated to be approximately 56.4 nm and 51.7 nm, respectively. According to Scherrer formula, the average grain size of  $n = \infty$  thick film is approximately 85.1 nm. Furthermore, with the decrease in  $n$  value, *i.e.*, the increase in organic interlayers, the low-angle diffraction peak shifts from 6.52° to 6.45° to the left. This shift is due to the lattice expansion caused by the increased content of organics, making the effect of organic cation-induced lattice expansion more pronounced.

### 3.2 Morphological characterization

To visually demonstrate the impact of the inorganic layer number  $n$  on the surface morphology of perovskite thick films, scanning electron microscopy (SEM) was employed to

characterize the surface and cross-sectional morphologies of the films. From Fig. 2(a) and (d), which respectively show the SEM surface and cross-sectional images for the  $n = \infty$  sample, it is observed that the grain size of the  $n = \infty$  thick film is uneven, with both large and small grains randomly distributed on the surface, leading to significant surface non-uniformity. The introduction of BA molecules can improve the wettability between the precursor solution of perovskite and the substrate (Fig. S2, ESI<sup>†</sup>), thereby achieving rapid spontaneous diffusion and surface infiltration of the solution on the substrate surface. This allows the solution to form a uniform liquid film on the substrate surface, avoiding the occurrence of liquid film shrinkage during solvent evaporation. Thanks to the wettability between the organic components and the substrate, the surfaces of  $n = 10$  (see Fig. 2(b) and (e)) and  $n = 6$  (see Fig. 2(c) and (f)) thick films become more uniform, exhibiting a layered structure similar to two-dimensional crystals, which visually verifies the existence of quasi-two-dimensional perovskites. Microscopic observations revealed that the  $n = 10$  sample surface and interface possess a layered crystal structure, indicating that the introduction of BA<sup>+</sup> successfully synthesized the quasi-two-dimensional perovskite structure. The quantity of

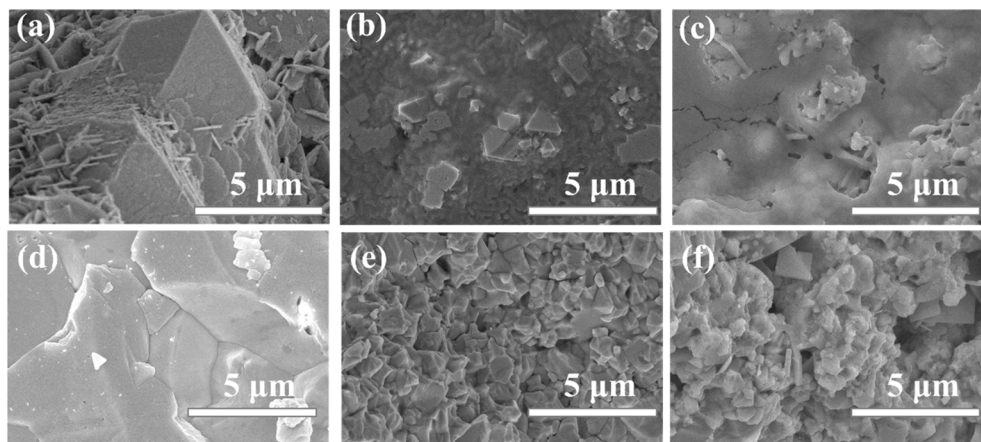


Fig. 2 (a–c) Top-view SEM images of perovskite about  $n = \infty$ ,  $n = 10$ , and  $n = 6$ , respectively; (d–f) cross-sectional SEM images of perovskite about  $n = \infty$ ,  $n = 10$ , and  $n = 6$ , respectively.



layered crystal structures in the  $n = 6$  sample is less than that in the  $n = 10$  sample, a phenomenon possibly due to organic polymers coating the grain surfaces. Despite some morphological differences between the  $n = 10$  and  $n = 6$  thick films, their grain sizes are both relatively small (Fig. 2 and S3, ESI†). This phenomenon can be attributed to the steric hindrance effect:<sup>28–30</sup> the organic cations not only regulate the dimensional structure but also significantly impact the crystallization kinetics of the film. Xiao and others<sup>31</sup> also noted that increasing the proportion of  $BA^+$  in the precursor solution provides numerous nucleation sites, significantly constraining the growth of perovskite particles. These findings are consistent with our observations.

### 3.3 Elemental distribution analysis

To further determine the changes and distribution of elements in the perovskite after dimension regulation using  $n$ -BABr, energy dispersive spectroscopy (EDS) tests were conducted on perovskite thick films of the three compositions. Elements such as Cs, Ag, Bi, and Br are evenly distributed in the selected regions of the sample, without significant agglomeration, as can be seen from Fig. 3.

From the elemental atomic content bar graph shown in Fig. 4, it is clearly demonstrated that with the decrease in  $n$  value, the contents of C and N elements in the perovskite thick films gradually increase, while the content of Cs decreases. Based on the XRD and SEM analyses above, it can be inferred

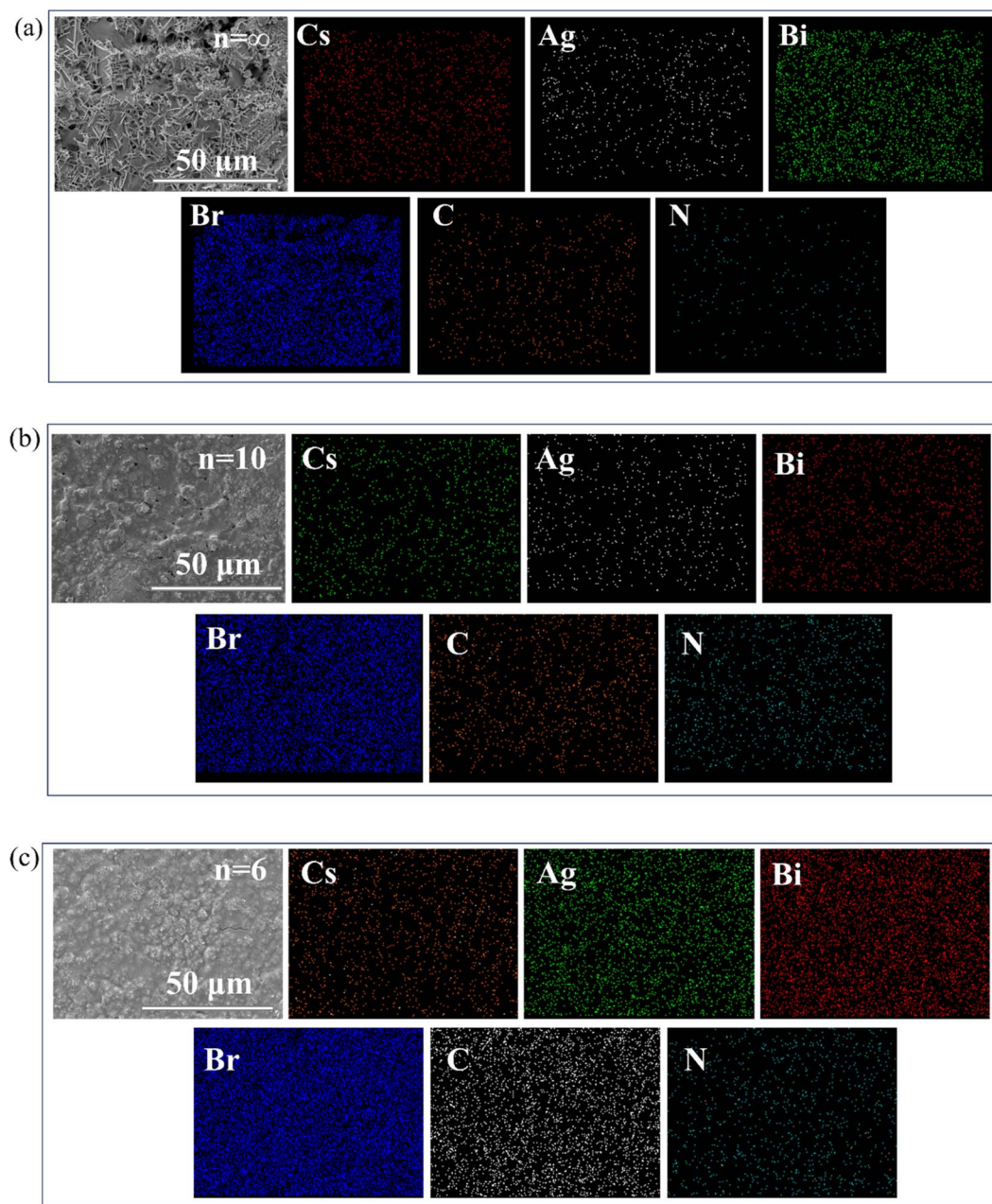


Fig. 3 EDS mapping of perovskite about (a)  $n = \infty$ , (b)  $n = 10$  and (c)  $n = 6$ .



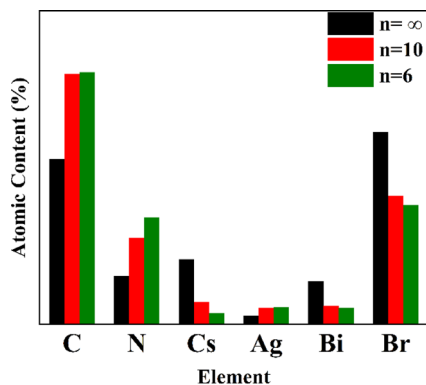


Fig. 4 Histogram of element contents of perovskite thick films about different  $n$  values.

that the organic cation  $\text{BA}^+$  has partially replaced the inorganic cation  $\text{Cs}^+$ , significantly affecting the overall structure of the material.

### 3.4 Resistivity

To study the suppression effect of the quasi-two-dimensional structure on ion migration, resistivity tests were first conducted on perovskites with different  $n$  values. As shown in Fig. 5, the current–voltage ( $I$ – $V$ ) characteristics curves obtained under dark test conditions for each material were fitted to slopes, and the resistivity was calculated according to the formula for resistivity. The test results show that after introducing a reasonable BA organic interlayer, the resistivity of the perovskite structure with an inorganic layer number of 10, *i.e.*, the  $n = 10$  component, was enhanced to  $1.75 \times 10^{10} \Omega \text{ cm}$ . The increase in resistivity is attributed to the dimensional regulation of the three-dimensional perovskite structure by the large organic molecules, effectively suppressing ion migration, reducing ionic conductivity, and lowering dark current. For the  $n = 6$  material, its resistivity was similar to that of the three-dimensional structure  $n = \infty$ , showing no significant improvement. Notably, the resistivity of the  $n = 6$  quasi-2D perovskite formed after introducing more  $\text{BA}^+$  remains almost unchanged compared to the three-dimensional perovskite. This is primarily

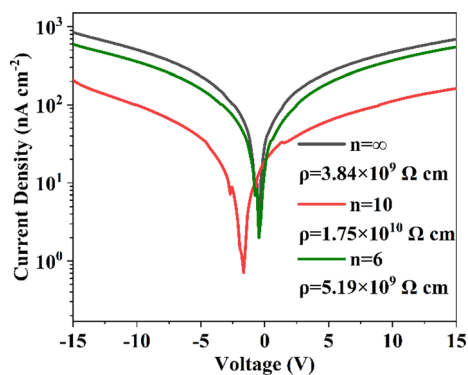


Fig. 5 Current–voltage ( $I$ – $V$ ) curves of perovskite thick films with different  $n$  values.

because the significant increase in the number of grain boundaries raises the defect density, creating channels for ion migration. This indicates that the negative impact of an increased number of grain boundaries due to the high proportion of  $\text{BA}^+$  partially offsets its ability to inhibit ion migration.

### 3.5 Ion migration characterization

To investigate the characteristics of dark current drift, the current–time ( $I$ – $t$ ) curves of all devices were tested under a single X-ray irradiation for 30 seconds at a bias electric field of  $160 \text{ V mm}^{-1}$ . As shown in Fig. 6, among all materials, the  $n = 10$  material exhibits the lowest dark current density, approximately  $66 \text{ nA cm}^{-2}$ . Defining the current drift value<sup>32</sup> as the difference in current density at the start and end points per unit time and per unit field strength, the degree and magnitude of current drift for different materials are quantified. The dark current drift values for  $n = 6$  and  $n = 10$  materials are less than those of the unmodified material devices, especially the  $n = 10$  material, which exhibits higher stability in terms of dark current, with relatively small dark current drift, only  $0.016 \text{ pA cm}^{-1} \text{ s}^{-1} \text{ V}^{-1}$ . This is comparable to other works involving quasi-two-dimensional materials, such as  $\text{PEA}_2\text{MA}_8\text{Pb}_9\text{I}_{28}$  (Table S1, ESI†). These results indicate that the quasi-two-dimensional structure shows a clear improvement in controlling dark current drift, *i.e.*, ion migration. Similarly to the dark current drift results, the  $n = 10$  material also exhibits relatively small current drift under X-ray irradiation, further validating the effectiveness of the quasi-two-dimensional structure in suppressing current drift. This particularly emphasizes its general applicability under different operating conditions.

To explore the dimension regulation from the perspective of ion migration mechanisms and deeply analyze the intrinsic ion migration mechanism, the conductivity of the thick film devices was calculated based on the  $I$ – $V$  curves in the high-temperature region. The degree of ion migration in the thick films was quantitatively analyzed using the Arrhenius equation related to temperature, with the ion migration activation energy  $E_a$  representing this characteristic. As shown in Fig. 7, for the control group  $n = \infty$  material, upon heating to 293 K, which enters the high-temperature region, the ion conductivity dominates the total conductivity, resulting in an  $E_a$  calculated to be 358 meV, consistent with other reports. For the quasi-two-dimensional structure of  $n = 10$  material treated with the large organic molecule *n*-BABr,  $E_a$  increased to 419 meV, indicating an ion migration activation energy increase of about 17%. The perovskite thick films modified with *n*-BABr show a significant suppression effect on ion migration, benefiting from the dimensional regulation by the large organic molecules. This effect constructs van der Waals gaps between layers, which restricts the migration of ions between layers.

### 3.6 X-ray detection test and analysis

For X-ray response testing, ITO/PVP/perovskite/Ag devices were placed under X-Rays with a photon energy of 80 keV, testing the photo-current and dark current under different doses and



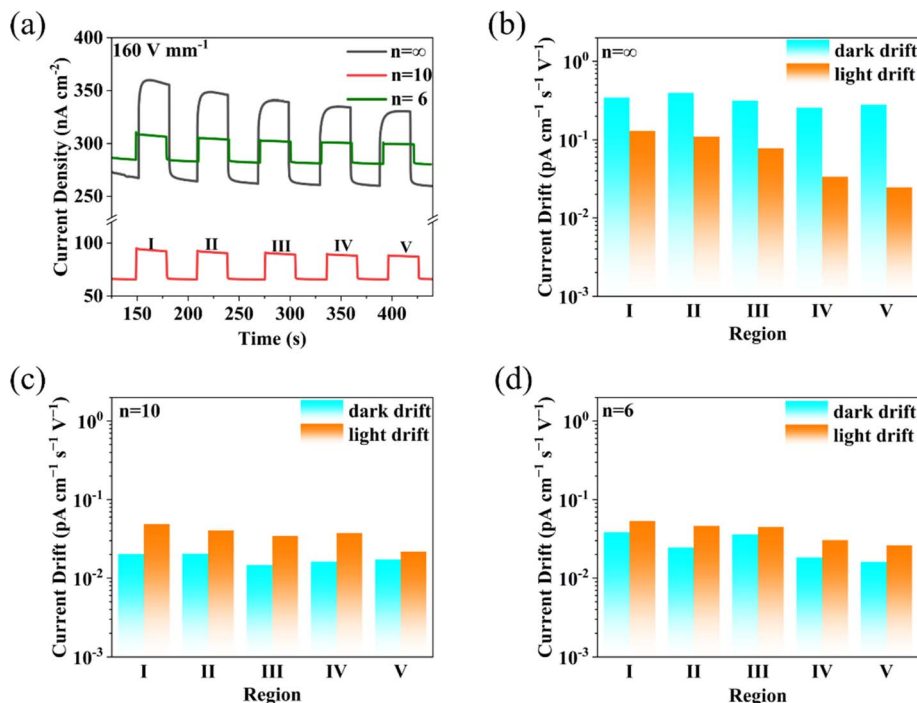


Fig. 6 Effect of dimensional regulation on the current drift of perovskite. (a) Current drift of perovskite with different  $n$  values; (b–d) the corresponding parameters of current drift.

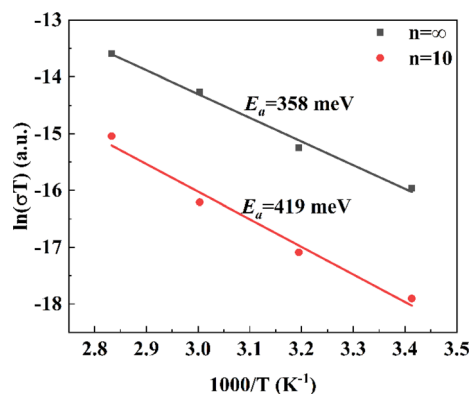


Fig. 7 Temperature-dependent conductivity test.

biases, thereby calculating parameters such as the device's X-ray sensitivity and detection limit.

The photocurrent-dose rate curves of the devices under different electric field strengths were tested and plotted as shown in Fig. 8(a). The slopes for each group were obtained using linear fitting, summarizing the X-ray sensitivity values of the devices as shown in Table 1. It was found that the device's sensitivity at an electric field strength of  $20 \text{ V mm}^{-1}$  was  $24.27 \mu\text{C Gy}_{\text{air}}^{-1} \text{ cm}^{-2}$ . To improve the device's response speed and carrier collection efficiency, applying a higher voltage under a certain dose rate of X-ray irradiation will produce a larger photo-response current, while the dark current remains stable, thereby achieving higher device sensitivity. The device approaches saturation under an electric field of  $400 \text{ V mm}^{-1}$ ,

with sensitivity reaching  $46.98 \mu\text{C Gy}_{\text{air}}^{-1} \text{ cm}^{-2}$ , twice that of amorphous selenium X-ray detectors ( $20 \mu\text{C Gy}_{\text{air}}^{-1} \text{ cm}^{-2}$ ). Further optimization of the thick film formation and crystal quality, improving carrier mobility, and suppressing ion migration, enable the device to operate at higher electric field strengths, potentially enhancing sensitivity to a higher level.

For X-ray detectors, the detection limit is also an important performance metric. As shown in Fig. 8(c), detection limit testing was performed for two types of devices under an electric field of  $320 \text{ V mm}^{-1}$ . By linear fitting of the signal-to-noise ratio for different doses, the detection limits for the two types of detectors were determined, with the  $n = 10$  detector having a detection limit of  $138 \text{ nGy}_{\text{air}} \text{ s}^{-1}$ , better than the  $n = \infty$  detector's  $2560 \text{ nGy}_{\text{air}} \text{ s}^{-1}$ . The detection limits of both types of X-ray detectors are low, with the  $n = 10$  detector being an order of magnitude lower than commercial amorphous selenium detectors (Table S1, ESI<sup>†</sup>), sufficient to meet standard medical diagnostic requirements, and close to the detection limit of  $59.7$  for  $\text{Cs}_2\text{AgBiBr}_6$  single crystal X-ray detectors (Table S1, ESI<sup>†</sup>), significantly reducing X-ray harm to the human body. The lower detection limit of X-ray detectors is due to lower dark current under comparable photo-current, which suppresses the device's noise current, thereby improving the signal-to-noise ratio and allowing the device to respond noticeably at smaller X-ray doses. The construction of quasi-two-dimensional structures suppresses ion migration, reducing ionic conduction and thereby achieving excellent X-ray detector performance in terms of detection limit.

Notably, the sensitivity of the device decreases after reasonable addition of  $n$ -BABr for dimension regulation of the three-



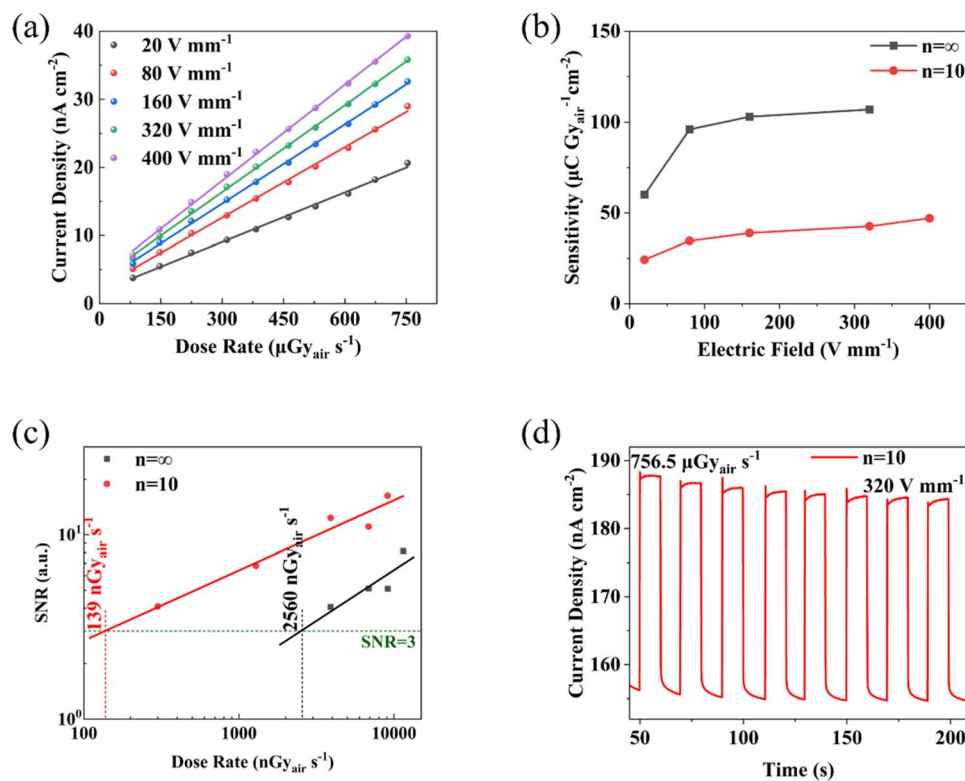


**Fig. 8** (a) Photocurrent density–dose curves of the  $n = 10$  under different electric field; (b) summary of the sensitivities of  $n = 10$  and  $n = \infty$  at different electric fields; (c) signal-to-noise ratio versus X-ray dose rate for  $n = 10$  and  $n = \infty$ , with the limit of detection obtained through linear fitting; (d) the cycle stability of  $n = 10$  device at  $320 \text{ V mm}^{-1}$  electric field (8 consecutive on–off cycles).

**Table 1** The X-ray sensitivities of  $n = 10$  device

Electric field $E/\text{V mm}^{-1}$	Sensitivity $S/\mu\text{C Gy}_{\text{air}}^{-1} \text{cm}^{-2}$	$R^2$ (%)
20	24.27	99.72
80	34.54	99.80
160	38.86	99.92
320	42.59	99.93
400	46.98	99.91

dimensional perovskite, as shown in Fig. 8(b). This phenomenon can be attributed to the hindrance of organic interlayers to the transport of photogenerated carriers<sup>33</sup> and the higher defect density and grain boundaries within the thick film affecting carrier transport. Thus, to some extent, it weakens the carrier collection efficiency, resulting in lower sensitivity compared to three-dimensional perovskite materials. In fact, compared to the significant optimization of dark current stability, this decrease in sensitivity performance is within an acceptable range.

Fig. 8(d) shows the detector's on/off cycling curve, used to test the device's cyclic stability performance. The test results indicate that the  $n = 10$  device maintains a stable dark current baseline under high electric field and long-term testing, with a slight reduction in photo-response current. This might be due to an increase in internal defects within the thick film under

high-energy X-ray irradiation, increasing the probability of carrier recombination and reducing photogenerated carriers.

## 4. Conclusion

In this work, a strategy of dimension regulation of lead-free perovskite three-dimensional structures using large organic molecules was adopted, and quasi-two-dimensional lead-free perovskite materials were prepared *via* an ultrasonic spray coating process. Thanks to the van der Waals gaps constructed by organic molecular layers, the movement of ions between perovskite layers was blocked, thereby reducing the ionic conductivity and stabilizing the device's dark and response currents. By rationally controlling the content of organic molecules, a material designated as  $n = 10$ , namely  $(\text{BA})_2\text{Cs}_9\text{Ag}_5\text{Bi}_5\text{Br}_{31}$ , was designed. This significantly enhanced the material's resistivity, effectively reduced dark current and current drift, increased the ion migration activation energy, and ensured long-term device stability. This provides a new perspective for the dimension regulation of lead-free polycrystalline perovskites and opens up broad prospects for their applications in X-ray detection and imaging.

## Data availability

The data supporting this article have been included as part of the ESI.†



## Conflicts of interest

There are no conflicts to declare.

## Acknowledgements

This work is supported by West China Hospital of Sichuan University-University of Electronic Science and Technology of China Medical and Industrial Integration Cross-Cultivation Project (ZYGX2022YGRH006), Project of Guangxi Key Laboratory of Superhard Materials (China Nonferrous Metal Guilin Research Institute of Geology for Mineral Resources) (No. 2023-K-01), the Research Foundation of Key Laboratory of New Processing Technology for Nonferrous Metal & Materials, Ministry of Education/Guangxi Key Laboratory of Optical and Electronic Materials and Devices (No. 22KF-23). The Sichuan Province Science and Technology Activities Funding for Returned Overseas Scholars. The authors also thank Shiyanjia Lab (<https://www.shiyanjia.com>) for the support of XRD and SEM test.

## References

- 1 S.-A. Zhou and A. Brahme, Development of phase-contrast X-Ray imaging techniques and potential medical applications, *Phys. Med. Eur. J. Med. Phys.*, 2008, **24**(3), 129–148.
- 2 A. Olivo, D. Chana and R. Speller, A preliminary investigation of the potential of phase contrast X-Ray imaging in the field of homeland security, *J. Phys. D: Appl. Phys.*, 2008, **41**(22), 225503.
- 3 P. Fromme and J. C. H. Spence, Femtosecond nanocrystallography using X-Ray lasers for membrane protein structure determination, *Curr. Opin. Struct. Biol.*, 2011, **21**(4), 509–516.
- 4 T. Masuzawa, I. Saito, T. Yamada, *et al.*, Development of an amorphous selenium-based photodetector driven by a diamond cold cathode, *Sensors*, 2013, **13**(10), 13744–13778.
- 5 W. Wei, Y. Zhang, Q. Xu, *et al.*, Monolithic integration of hybrid perovskite single crystals with heterogenous substrate for highly sensitive X-Ray imaging, *Nat. Photonics*, 2017, **11**(5), 315–321.
- 6 Y. Liu, Z. Xu, Z. Yang, *et al.*, Inch-size 0d-structured lead-free perovskite single crystals for highly sensitive stable X-Ray imaging, *Matter*, 2020, **3**(1), 180–196.
- 7 A. Raj, M. Kumar, A. Kumar, *et al.*, Investigating the potential of lead-free double perovskite  $\text{Cs}_2\text{AgBiBr}_6$  material for solar cell applications: A theoretical study, *Int. J. Energy Res.*, 2022, **46**(10), 13801–13819.
- 8 Z. Li, F. Zhou, H. Yao, *et al.*, Halide perovskites for high-performance X-Ray detector, *Mater. Today*, 2021, **48**, 155–175.
- 9 T. Yang, F. Li and R. Zheng, Recent advances in radiation detection technologies enabled by metal-halide perovskites, *Mater. Adv.*, 2021, **2**(21), 6744–6767.
- 10 H. Wei and J. Huang, Halide lead perovskites for ionizing radiation detection, *Nat. Commun.*, 2019, **10**(1), 1066.
- 11 H. Wu, Y. Ge, G. Niu, *et al.*, Metal halide perovskites for X-Ray detection and imaging, *Matter*, 2021, **4**(1), 144–163.
- 12 W. Pan, H. Wu, J. Luo, *et al.*,  $\text{Cs}_2\text{AgBiBr}_6$  single-crystal X-Ray detectors with a low detection limit, *Nat. Photonics*, 2017, **11**(11), 726–732.
- 13 W. Qian, X. Xu, J. Wang, *et al.*, An aerosol-liquid-solid process for the general synthesis of halide perovskite thick films for direct-conversion X-Ray detectors, *Matter*, 2021, **4**(3), 942–954.
- 14 B.-w Park and S. I. Seok, Intrinsic instability of inorganic-organic hybrid halide perovskite materials, *Adv. Mater.*, 2019, **31**(20), 1805337.
- 15 H. Li, X. Shan, J. N. Neu, *et al.*, Lead-free halide double perovskite-polymer composites for flexible X-Ray imaging, *J. Mater. Chem. C*, 2018, **6**(44), 11961–11967.
- 16 M. Xia, Z. Song, H. Wu, *et al.*, Compact and large-area perovskite films achieved via soft-pressing and multi-functional polymerizable binder for flat-panel X-Ray imager, *Adv. Funct. Mater.*, 2022, **32**(16), 2110729.
- 17 D. Meggiolaro, E. Mosconi and F. De Angelis, Formation of surface defects dominates ion migration in lead-halide perovskites, *ACS Energy Lett.*, 2019, **4**(3), 779–785.
- 18 B. Yang, W. Pan, H. Wu, *et al.*, Heteroepitaxial passivation of  $\text{Cs}_2\text{AgBiBr}_6$  wafers with suppressed ionic migration for X-Ray imaging, *Nat. Commun.*, 2019, **10**, 1989.
- 19 H. Tsai, S. Shrestha, L. Pan, *et al.*, Quasi-2d perovskite crystalline layers for printable direct conversion X-Ray imaging, *Adv. Mater.*, 2022, **34**(13), 2106498.
- 20 Y. Li, Y. Lei, H. Wang, *et al.*, Two-dimensional metal halides for X-Ray detection applications, *Nano-Micro Lett.*, 2023, **15**(1), 128.
- 21 Z. Xu, X. Liu, Y. Li, *et al.*, Exploring lead-free hybrid double perovskite crystals of  $(\text{BA})_2\text{CsAgBiBr}_7$  with large mobility-lifetime product toward X-Ray detection, *Angew. Chem., Int. Ed.*, 2019, **58**(44), 15757–15761.
- 22 G. J. Yukta, M. A. Afroz, *et al.*, Efficient and highly stable X-Ray detection and imaging using 2D  $(\text{BA})_2\text{PbI}_4$  perovskite single crystals, *ACS Photonics*, 2022, **9**(11), 3529–3539.
- 23 M. Zhang, D. Xin, S. Dong, *et al.*, Methylamine-assisted preparation of ruddlesden-popper perovskites for stable detection and imaging of X-Rays, *Adv. Opt. Mater.*, 2022, **10**(23), 2201548.
- 24 X. Zhang, T. Zhu, C. Ji, *et al.*, In situ epitaxial growth of centimeter-sized lead-free  $(\text{BA})_2\text{CsAgBiBr}_7/\text{Cs}_2\text{AgBiBr}_6$  heterocrystals for self-driven X-Ray detection, *J. Am. Chem. Soc.*, 2021, **143**(49), 20802–20810.
- 25 B. A. Connor, L. Leppert, M. D. Smith, *et al.*, Layered halide double perovskites: Dimensional reduction of  $\text{Cs}_2\text{AgBiBr}_6$ , *J. Am. Chem. Soc.*, 2018, **140**(15), 5235–5240.
- 26 X. He, M. Xia, H. Wu, *et al.*, Quasi-2d perovskite thick film for X-Ray detection with low detection limit, *Adv. Funct. Mater.*, 2021, **32**(7), 2109458.
- 27 S. Khare and J. V. Gohel, Performance enhancement of cost-effective mixed cationic perovskite solar cell with  $\text{MgCl}_2$  and n-BAI as surface passivating agents, *Opt. Mater.*, 2022, **132**, 112845.
- 28 J. Gong, M. Hao, Y. Zhang, *et al.*, Layered 2D halide perovskites beyond the Ruddlesden-Popper phase: Tailored



- interlayer chemistries for high-performance solar cells, *Angew. Chem., Int. Ed.*, 2022, **61**(10), e202112022.
- 29 Y. Miao, M. Ren, H. Wang, *et al.*, Surface termination on unstable methylammonium-based perovskite using a steric barrier for improved perovskite solar cells, *Angew. Chem., Int. Ed.*, 2023, **62**(51), e202312726.
- 30 D. He, R. Li, B. Liu, *et al.*, Unraveling abnormal buried interface anion defect passivation mechanisms depending on cation-induced steric hindrance for efficient and stable perovskite solar cells, *J. Energy Chem.*, 2023, **80**, 1–9.
- 31 Z. Xiao, R. A. Kerner, L. Zhao, *et al.*, Efficient perovskite light-emitting diodes featuring nanometre-sized crystallites, *Nat. Photonics*, 2017, **11**(2), 108–115.
- 32 C. Xue, Y. Xiao, X. Liu, *et al.*, Realizing low-ion-migration and highly sensitive X-Ray detection by building g-C<sub>3</sub>N<sub>4</sub> and ch<sub>3</sub>nh<sub>3</sub>pbi<sub>3</sub> bulk heterojunction pellets, *J. Mater. Chem. A*, 2023, **11**(47), 25918–25928.
- 33 D. Xin, M. Zhang, Z. Fan, *et al.*, A-site cation engineering of Ruddlesden–Popper perovskites for stable, sensitive, and portable direct conversion X-Ray imaging detectors, *J. Phys. Chem. Lett.*, 2022, **13**(51), 11928–11935.

